Atmospheric Acoustic Interferometer Tomography of Temperature and Winds

STUART BRADLEY[1], SABINE VON HÜNERBEIN, AND ANNEKE HADDAD

School of Acoustics and Electronic Engineering, University of Salford, Salford, UK

[1] *Corresponding author address:* Stuart G Bradley, School of Acoustics and Electronic Engineering, University of Salford, Salford M5 4WT, UK. E-mail: S.G.Bradley@salford.ac.uk

Abstract

A technique is described for multiple-path propagation time measurements in the surface layer of the atmosphere. This is based on solving simple bi-directional ray tracing equations on successively higher penetrating paths using propagation times for a short acoustic pulse. The scattering process from turbulence is shown to be capable of providing signals from which phase comparisons can be made and time-of-flight deduced. Simulations demonstrate that the method has potential for deriving continuous temperature and wind profiles.

In practice a multiple-beam interferometer can be used at each end of the path. Such an instrument has been designed and first results will be given, together with future planned enhancements.

Keywords: Temperature profiles, acoustic propagation, sound speed profile, acoustic interferrometer

1. Introduction

Acoustic time of flight measurements have been used successfully by Arnold et al (1999) to obtain temperature and wind information. They used direct line-of-sight with a transmitter at one end of the propagation path and a receiver at the other end. The principle of the present acoustic interferometer is transmitting a pulse of sound at an oblique angle and measuring the time-of-flight of the sound reflected from turbulent patches. By progressively increasing the elevation of the directional transmitter and reflector, the ray paths of sound can be estimated, allowing for temperature and wind profiles to be deduced. In order to obtain both wind and temperature, it is necessary to transmit from either end of a baseline.

Brown et al. (1978) made measurements of pulse propagation time using a simple acoustic interferometer and demonstrated potential of the method. However, Ostashev (1984) concluded that time intervals could not be measured sufficiently well, even for the zero-wind case, given the diffuse nature of acoustic returns.

We describe the acoustic design and implementation using small piezo speakers in a linear phased array. The design was validated in an anechoic chamber. A major part of this preliminary investigation is, however, to understand the equations giving time-of-flight so that they can be inverted to give refractive index. We show that it is relatively straight-forward to retrieve temperatures in the absence of wind shear, but the system of equations becomes more complex in the general case. We review Ostashev's finding, given advances in acoustic technology.

2. Phase of turbulent scattering

Previous treatments have assumed no phase shift effects due to the random nature of turbulence or to the scattering of sound from turbulence. Since this is a central assumption, we first examine the phase of turbulent scattering. The theory has been thoroughly treated by Tartarski (1961) and many others, so we give an abbreviated coverage here, concentrating on amplitude rather than intensity. Scattering from turbulence satisfies an acoustic wave equation with the strength of scattering dependent on refractive index variation n'

$$\frac{n'}{n} = \frac{k\underline{v'} \bullet \underline{\hat{r}}}{c} + \frac{T'}{2T} \tag{1}$$

where n is the refractive index, $\underline{\hat{r}}$ is the unit vector in the direction of $\underline{r}$ from the source to the scatterers, k is the wavenumber, $\underline{v'}$ is the turbulent velocity variation, c the speed of sound, and T and T' the temperature and temperature variation respectively. When adding contributions from scatterers S_1, S_2, ….. (see Fig. 1), the correct phase for S_j is taken into account by allowing for phase path

$$k\left(\underline{r'_j} \bullet \underline{\hat{r}} + r + r'_{oj}\right)$$

where

$$\underline{r_{oj}}' = \underline{r_o} - \underline{r'_j} \quad . \tag{2}$$

For the origin close to the scatterers and with observations at a large distance,

$$r'_{oj} \approx r_o - \underline{r'_j} \bullet \underline{\hat{r}_o} \tag{3}$$

where $\underline{\hat{r}_o}$ is the unit vector in the direction of $\underline{r_o}$. The phase is therefore

$$k\underline{r'_j} \bullet \left(\underline{\hat{r}} - \underline{\hat{r}_o}\right) + k\left(r + r_o\right) \quad .$$

At a large distance r_o compared with dimensions H of the scattering volume, the angular dependence of scattering from all scatterers will be ≈ same, say $f(\theta)$, where $\theta \approx \cos\left(\underline{\hat{r}} \bullet \underline{\hat{r}_o}\right)$.

Allowing for the 1/r factor for amplitude fall-off, the amplitude will have the form

$$A \quad = \quad f(\theta)\frac{e^{ik(r+r_o)}}{nrr_o}\eta(k) \tag{4a}$$

where

$$\eta(k) \quad = \quad \iint_V n'(x,z)e^{ikr'\bullet(\hat{r}-\hat{r}_o)}dx\,dz \tag{4b}$$

where (x,z) are the Cartesian coordinates within the scattering volume V. The usual treatment is to consider intensities, proportional to A^*A, which involve correlation functions $\overline{n'(x_1,z_1)n'(x_2,z_2)}$. Here we are interested in the phase contribution from scattering, and therefore the amplitude.

For back-scatter, $\hat{r}$ is in the positive z direction and r_o in the negative z direction, giving

$$\eta(k) \quad = \quad \int_{-\frac{H}{2}}^{\frac{H}{2}} n'_z(z)e^{i2kz}dx\,dz \quad = \quad N'_z(2k) * \mathrm{sinc}(Hk) \tag{5}$$

where $n'_z(z)$ is the integral of $n'(x,z)$ over x, and $N'_z(2k)$ is its Fourier transform. The amplitude is therefore sensitive to scattering from fluctuations of scales $\approx 2k \pm 1/H$. However, the fluctuations are random, and so the volume-averaged phase contribution of η will be zero. This means that the phase observed will be due to the $e^{ik(r+r_o)}$ term in (4a): this is just the phase path to the scattering volume and back to the receiver. For transmission at zenith angle θ and reception at zenith angle ϕ similar results are obtained, with sensitivity to horizontal scales of $k(\sin\theta + \sin\phi)$ and vertical scales of $k(\cos\theta + \cos\phi)$. The conclusions regarding phase are unaltered. Consequently we need only consider the geometric phase path in considering propagation times.

3. Acoustic design

A number of sensors were examined: the Sonitron SCS17, 24, 57 and 77 (the numeric code gives the diameter of the speaker), and the Motorola KSN1001A, a super-horn of diameter *d* = 85 mm. Some results from the super-horn will be given, since it has the highest output power and superior signal-to-noise. The single-speaker response is quite broad, which is required for wide steering of zenith angles in a phased array (Fig. 2).

Simulations were conducted for different numbers of speakers and at various spacings *L* and wavelength λ. Figure 3 shows an array pattern for 12 speakers spaced at 2.5 wavelengths. The peaks should appear at $\theta = \sin^{-1}\left(m\frac{\lambda}{L}\right)$ for *m* = 0, ±1, ±2,… and for inter-speaker spacing *L*. Calculated angles in the table agree closely with measurements. Note that the aim is to retain a number of diffraction grating side-lobes, whereas usual SODAR design is to suppress these. The multiple-lobe structure allows for the possibility of simultaneously recording multiple path times of flight, with a bi-static arrangement consisting of two such linear arrays. Alternatively, speaker spacing can be chosen to give a single lobe which is steered in conventional fashion by appropriate phasing. The difficulty here is in obtaining low-angle beams.

4. Ray tracing for zero wind

4.1 *The lowest layer (n =1)*

The curvature of the ray is very small for typical temperature profiles: after travelling 30 m a ray at 25° to the vertical has only deviated by 20 cm if the lapse rate is 0.05^{o}C m^{-1}. Time-of-flight methods are therefore necessary. Ostashev (1984) has described obtaining the integral of sound speed over the propagation path in the no-wind, small temperature deviation

case. Ultimately use of his method requires discretization, so we consider the case of slabs of homogeneous atmosphere as an approximation to the continuous case. Consider transmission upward at zenith angle θ_{11} and reception at zenith angle ϕ_{11} distance D away. Here the first subscript refers to the interrogating beam, with 1 for the lowest elevation, 2 for the next highest elevation, and so on. The second subscript refers to the layer the beam is passing through, 1 for the lowest, 2 for the next highest, and so on. The strategy is to consider transmission at the lowest elevation first, measuring time-of-flight t_1, and inferring the sound speed in layer 1. Then a higher elevation beam is used to infer the sound speed in layer 2 from the time-of-flight t_2, using the known sound speed v_1 in layer 1. The layer thickness, h_n, are established from the ray trace of the n^{th} beam.

From Fig. 4,

$$D = v_1(t_l \sin\theta_{11} + t_r \sin\phi_{11}) \tag{2a}$$

$$t_l \cos\theta_{11} = t_r \cos\phi_{11} \tag{2b}$$

$$t_1 = t_l + t_r \tag{2c}$$

giving

$$D = v_1 t_1 \frac{\sin(\theta_{11} + \phi_{11})}{\cos\theta_{11} + \cos\phi_{11}} \tag{3a}$$

and

$$h_1 = \frac{D}{\tan\theta_{11} + \tan\phi_{11}} \tag{3b}$$

from which v_1 can be found.

4.2 *Successive layers (n = 2, 3,…)*

We measure

$$D = v_{n-1}\left(t_a \sin\theta_{n,n-1} + t_d \sin\phi_{n,n-1}\right) + v_n\left(t_b \sin\theta_{n,n} + t_c \sin\phi_{n,n}\right) \quad (4a)$$

and

$$t_n = t_a + t_b + t_c + t_d\,. \quad (4b)$$

From previous layers we know v_{n-1}, $\theta_{n,n-1}, \phi_{n,n-1}$, and h_{n-1} leaving 7 unknowns:

$t_a \quad t_b \quad t_c \quad t_d \quad v_n \quad \theta_{n,n} \quad \phi_{n,n}$. Based on Fig. 5 and Snell's Law, and appropriate algebra, for layer *n*, (*n* = 2, 3,….),

$$D = \sum_{i=1}^{n-1} h_i\left(\tan\theta_{ni} + \tan\phi_{ni}\right) + \mu_n^2 v_{n-1}\left[t_n - t^*\right]a_n \quad (5a)$$

where

$$t^* = \sum_{i=1}^{n-1} \frac{h_i}{v_i}\left(\frac{1}{\cos\theta_{ni}} + \frac{1}{\cos\phi_{ni}}\right), \quad (5b)$$

$$a_n = \left[\frac{\sin\theta_{nn-1} + \alpha_n \sin\phi_{nn-1}}{1+\alpha_n}\right], \quad (5c)$$

$$\mu_n = \frac{v_n}{v_{n-1}} \quad (5d)$$

and

$$\alpha_n = \left[\frac{1-\left(\mu_n \sin\theta_{nn-1}\right)^2}{1-\left(\mu_n \sin\phi_{nn-1}\right)^2}\right]^{\frac{1}{2}}. \quad (5e)$$

From (5a-e) one can solve progressively for μ_n, *n* = 2,3,…

4.3 *Simulation of temperature retrievals*

A simulation was run with the layer and beam structure shown in Fig. 6. Various combinations of 0°, 25° and 55° were used for beam zenith angles. The propagation times for the 5 beam combinations and temperatures were first found. A random error of 0.1 ms was introduced to these times and the inverse procedure used to find layer heights and temperatures. The rms error in retrieved temperature was 0.2°. For an interrogating frequency of 5000 Hz, this time measurement error amounts to ½ cycle. In practice it should not be difficult to measure phase delays to better than 1/36 cycle (10°): in that case the rms temperature error is 0.015°C.

5. Temperature and wind estimates

The problem with profiling in the presence of both temperature and wind gradients is that the sound speed is a function of direction, and this introduces further variables.

5.1 *System of equations*

For the first layer there are the measurements of transmitted and reception angles and time of flight for both upwind and downwind directions: there are two unknowns v and wind speed w and the two measured travel times. A set of 12 equations based on simple geometry gives the unknown layer height, sound speed and wind speed, as well as upward and downward travel times, propagation angles and propagation speeds. Each successive layer has a similar set of equations, with the addition of two Snell's Law equations to give the two new ray angles at the base of the layer.

5.2 *Temperature and wind retrievals*

A simulation was again run with the parameters shown in Fig. 6 and with winds of 1, 1.5, 1, 0, and –1 m s^{-1} from the lowest to highest layers. This gave

$$\frac{dT}{dt} = 5 \times 10^3 \text{ K s}^{-1} \qquad \frac{dv}{dt} = 6 \times 10^3 \text{ m s}^{-2}$$

for the errors in estimated temperature T and wind speed v for given measurement errors in time of flight t. A measurement error of 0.1 ms in time of flight therefore gives rms errors of 0.5 K and 0.6 m s^{-1} for temperature and speed. Because the deviations of the sound path are very small, the predicted errors in estimated layer heights are negligible.

6. Practical implementation

The above treatment suggests there may be a practical application for the method. A bi-static arrangement is required, however, and a substantial baseline is necessary to allow good angle definition. Furthermore, a triangular system of sensors is required to obtain wind vectors. This limits the sites in which such a system could be used. Nevertheless, the potential exists for continuous profiling of wind and temperature on flat land using relatively inexpensive apparatus. Note that only arrival times are required and not signal strength or frequency. This lends itself to a simple phase-locked-loop detection method.

Brown et al (1978) obtained measurements using a bi-static SODAR and a facsimile output. One such plot is reproduced in Fig. 7 with the dark bands showing arrivals from different beams in a multiple-beam interferometer. This demonstrates practical feasibility using more limited technology than presently available.

A prototype system consisting of a linear array of speakers has been constructed and is undergoing field trials. This has the flexibility of the speakers being mounted on rails so speaker spacing can be readily changed, as shown in Fig. 8.

Ostashev (1984) concluded that propagation speed methods for temperature retrievals were unlikely to be successful. This was based on detecting the leading edge of a pulse from a system having a beam width of 2°, where the range of ray paths over the beam width leads to a diffuse pulse arrival. Modest speaker arrays can achieve such narrow beam widths (see Fig. 3). However, much improved phase measurements are possible if the information contained in the whole pulse is used. For example, Bradley et al (2001) have measured phase returns from conventional phased-array SODARs to much better accuracy than possible by using the pulse leading edge. The phase-encoded pulse system described by Bradley (1999) has the capability of optimising the information available in the 400-500 cycles typically available in a pulse. In this case it is necessary to perform a Doppler search, since the pulse is significantly compressed or extended by Doppler shift in typical atmospheric situations. The theoretical phase limitation if phase is modulated on a half-wavelength basis is better than 0.5°. This technique in itself gives an alternate measure of wind speed, and so provides added redundancy.

REFERENCES

Arnold K., A. Ziemann and A. Raabe, 1999: Acoustic tomography inside the atmospheric boundary layer. *Phys. Chem. Earth* (B) **24**, 133-137

Bradley, S. G., 1999: Use of coded waveforms for SODAR systems. *Met. Atmos. Phys.,* **67**, 15-24.

Bradley, S. G., V. J. Hipkin and K. Underwood, 2001: The relationship between the phase of a sodar signal and atmospheric temperature. In Press: JTECH MS#20081402B

Brown, E. M., C. G. Little, and W. M. Wright, 1978: Echosonde interferometer for atmospheric research. *J. Acoust. Soc. Am.*, **63**, 694-699.

Ostashev, V. E., 1984: Possibility of reconstructing vertical profiles of the velocity of sound in a bistatic scheme of acoustic sounding of the atmosphere and the ocean. *Izvestiya, Atmos. Ocean. Phys.*, **20**, 147-150.

Tatarski, V. I., 1961: Wave propagation in a turbulent medium. *Dover, New York*, 285pp.

Figure captions

FIG. 1. Scattering geometry.

FIG. 2. Angular beam pattern for a single speaker.

FIG. 3. Array of 12 speakers spaced at $L = 2.5\ \lambda$.

FIG. 4. Single layer ray trace.

FIG. 5. Rays in layer n-1 and layer n.

FIG. 6. Profile simulation parameters.

FIG. 7. Detail from Brown et al. (1978) showing dark bands on a facsimile trace due to individual arrivals.

FIG. 8. Adjustable linear array configuration.

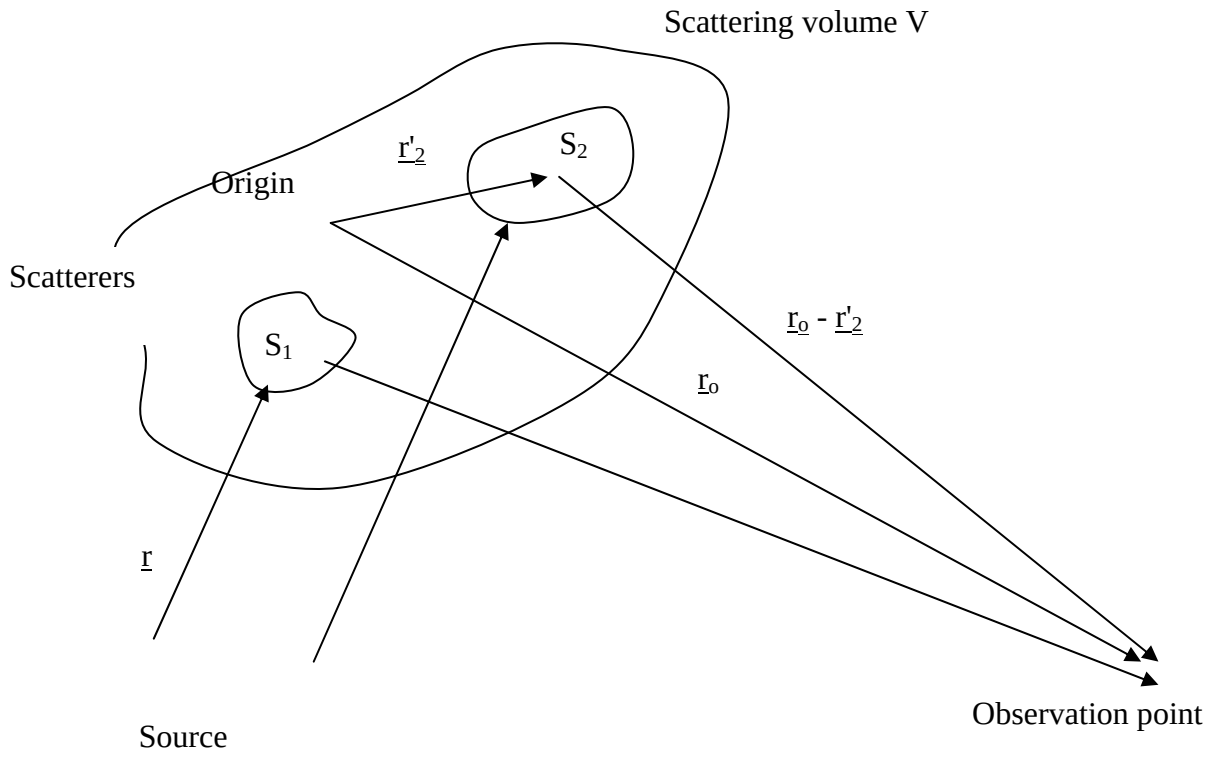

FIG. 1. Scattering geometry.

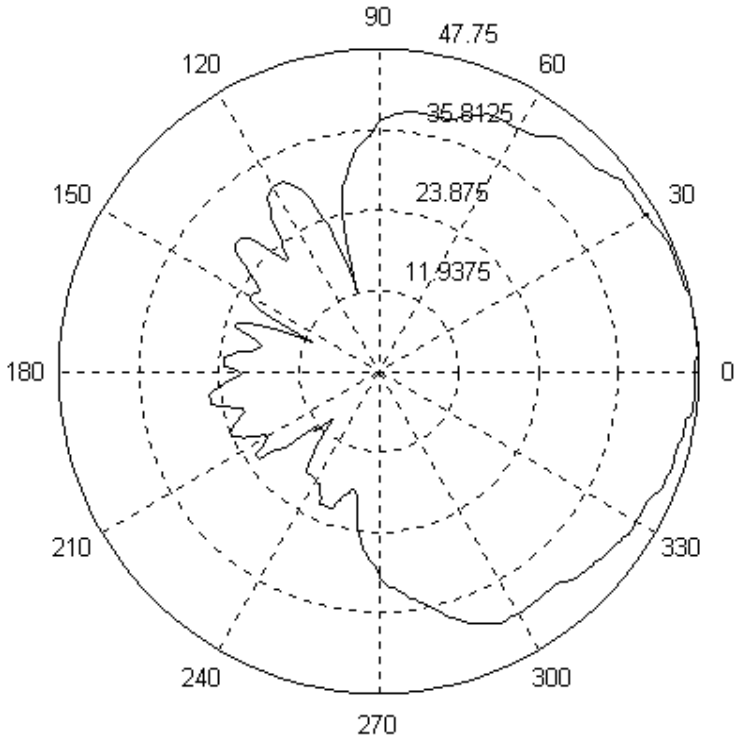

FIG. 2. Angular beam pattern for a single speaker.

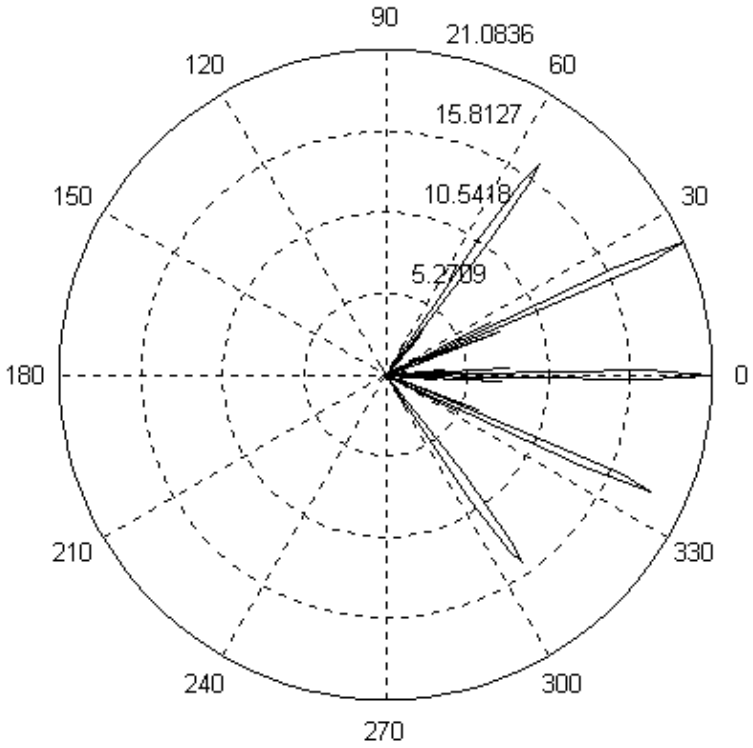

FIG. 3. Array of 12 speakers spaced at $L = 2.5\ \lambda$.

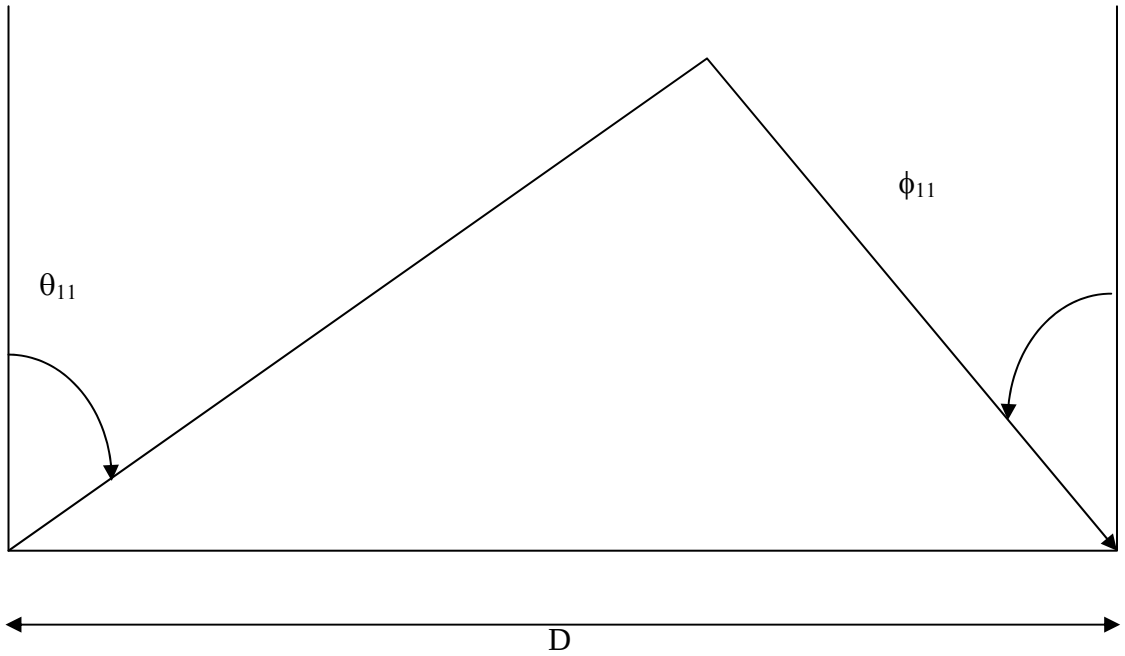

FIG. 4. Single layer ray trace.

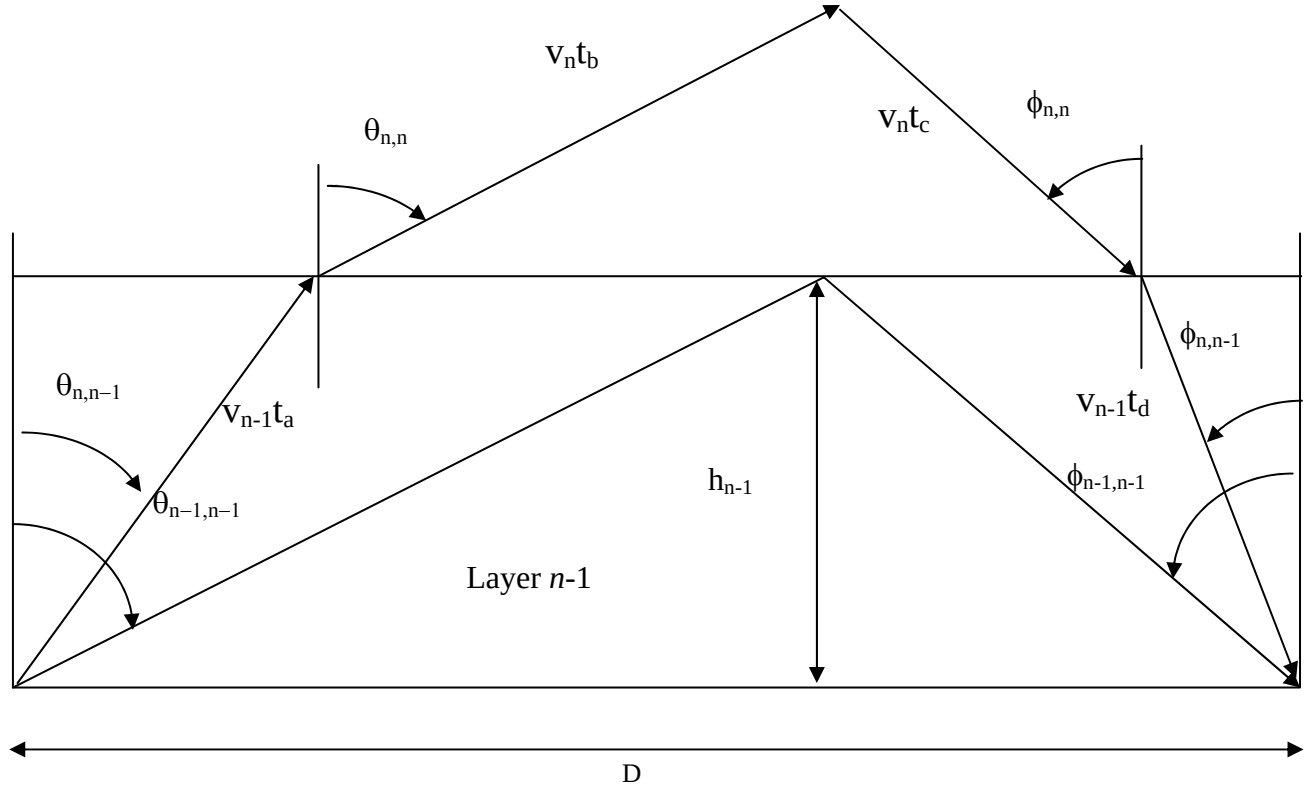

FIG. 5. Rays in layer *n*-1 and layer *n*.

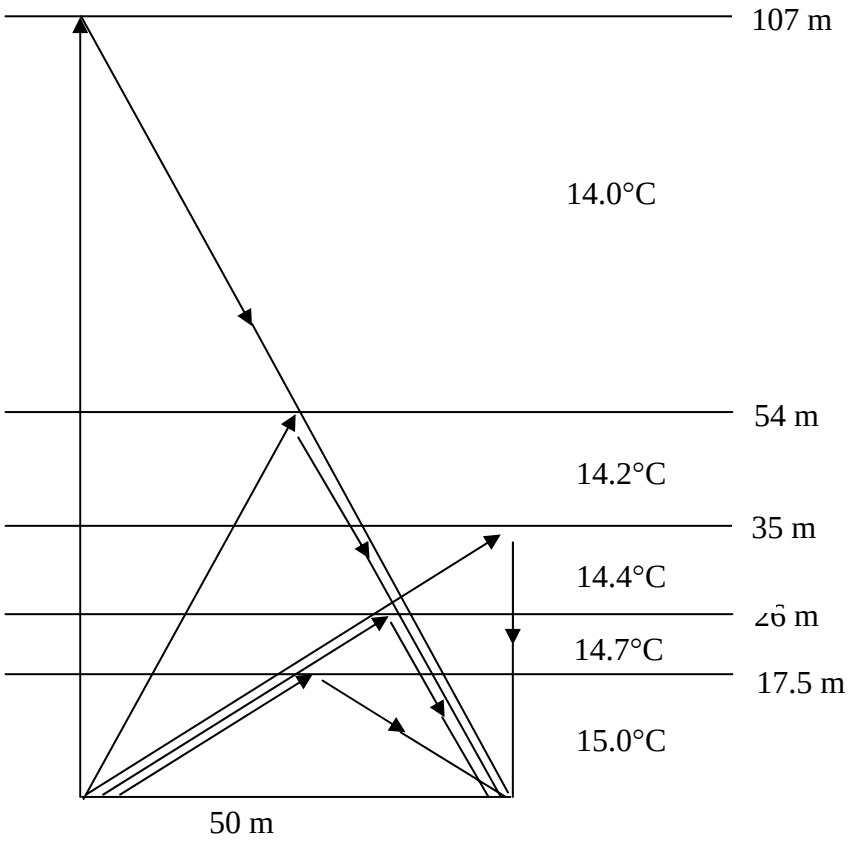

FIG. 6. Profile simulation parameters.

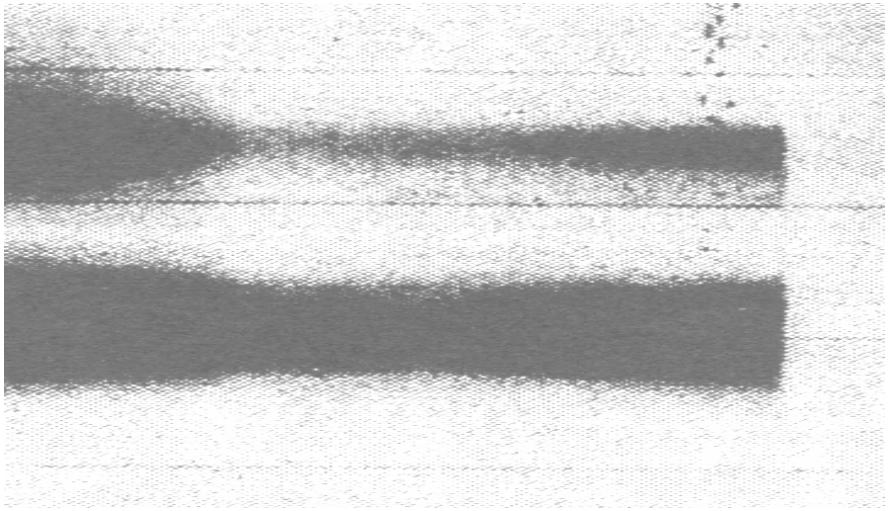

FIG. 7. Detail from Brown et al. (1978) showing dark bands on a facsimile trace due to individual arrivals.

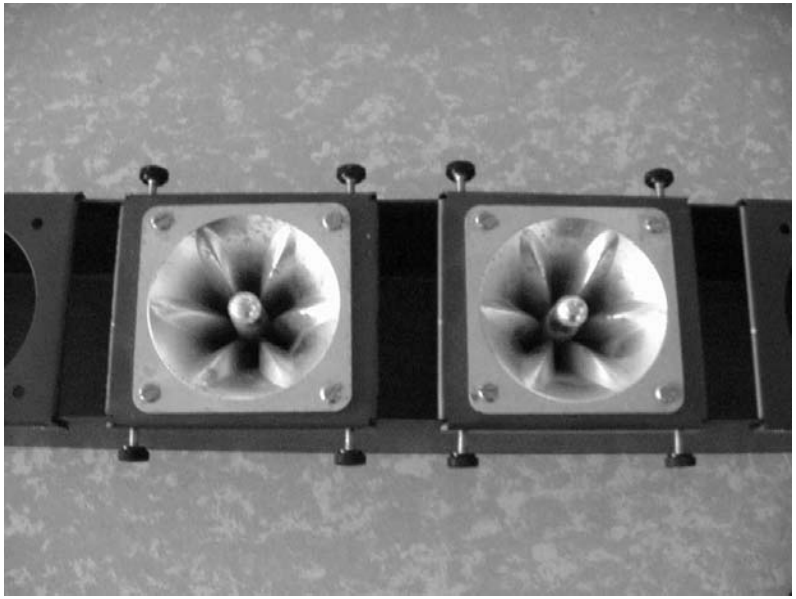

FIG. 8. Adjustable linear array configuration.